

BS-LDM: Effective Bone Suppression in High-Resolution Chest X-Ray Images with Conditional Latent Diffusion Models

Yifei Sun, Zhanghao Chen, Hao Zheng, Wenming Deng, Jin Liu, Wenwen Min, Ahmed Elazab, Xiang Wan, Changmiao Wang, Ruiquan Ge, *Member, IEEE*

Abstract—Lung diseases represent a significant global health challenge, with Chest X-Ray (CXR) being a key diagnostic tool due to their accessibility and affordability. Nonetheless, the detection of pulmonary lesions is often hindered by overlapping bone structures in CXR images, leading to potential misdiagnoses. To address this issue, we developed an end-to-end framework called BS-LDM, designed to effectively suppress bone in high-resolution CXR images. This framework is based on conditional latent diffusion models and incorporates a multi-level hybrid loss-constrained vector-quantized generative adversarial network which is crafted for perceptual compression, ensuring the preservation of details. To further enhance the framework's performance, we introduce offset noise and a temporal adaptive thresholding strategy. These additions help minimize discrepancies in generating low-frequency information, thereby improving the clarity of the generated soft tissue images. Additionally, we have compiled a high-quality bone suppression dataset named SZCH-X-Rays. This dataset includes 818 pairs of high-resolution CXR and dual-energy subtraction soft tissue images collected from a partner hospital. Moreover, we processed 241 data pairs from the JSRT dataset into negative images, which are more commonly used in clinical practice. Our comprehensive experimental and clinical evaluations reveal that BS-LDM excels in bone suppression, underscoring its signifi-

cant clinical value.

Index Terms—Chest X-ray, bone suppression, conditional latent diffusion model, dual-energy subtraction, supervised learning.

I. INTRODUCTION

LUNG disease remains a leading cause of high morbidity and mortality worldwide [1], [2]. Chest X-Ray (CXR) is the primary imaging technique for evaluating conditions such as inflammation, tuberculosis, and lung masses owing to its accessibility, cost-effectiveness, and low radiation exposure. However, even skilled radiologists may miss lesions in CXR images. This challenge primarily arises from bone structures overlapping with the lung region, which can obscure crucial details necessary for accurate detection and diagnosis. Research indicates that between 82% and 95% of undetected lung cancers are concealed by these bone structures [3]. Consequently, bone suppression techniques in CXR images could greatly aid radiologists and enhance the performance of computer-aided pulmonary lesion detection [4], [5].

Dual-Energy Subtraction (DES) imaging is a technique used to reduce visual clutter in CXR images caused by overlapping bone structures [6]. DES radiography uses two X-ray exposures at different energy levels to create two separate radiographs. These are then combined to produce a single image that emphasizes either soft tissue or bone structures. For soft tissue imaging, removing the bone component significantly enhances the clarity of chest radiographs. However, DES imaging requires specialized equipment and results in higher radiation doses, which limits its accessibility and use in developing and low-income countries. This limitation poses challenges in acquiring high-quality DES soft tissue images.

An alternative to DES imaging for bone suppression in CXR images is image processing, which does not require specialized equipment. Traditional image processing approaches treat bone suppression as a regression prediction problem, using supervised methods. For instance, Suzuki *et al.* [7] utilized a multi-task artificial neural network to generate bone images from CXR images, allowing for the subtraction of these bone images to yield soft tissue images. However, the small dataset used limited the generalizability of their approach. Following this, statistical analysis methods were developed

This work was supported by the Open Project Program of the State Key Laboratory of CAD&CG, Zhejiang University (No. A2410), Zhejiang Provincial Natural Science Foundation of China (No. LY21F020017), National Natural Science Foundation of China (No. 61702146, 62076084, U22A2033, U20A20386), Guangdong Basic and Applied Basic Research Foundation (No. 2022A1515110570), Innovation Teams of Youth Innovation in Science and Technology of High Education institutions of Shandong Province (No. 2021KJ088). (Corresponding author: Changmiao Wang, Ruiquan Ge).

Y. Sun, Z. Chen, H. Zheng and R. Ge are with Hangzhou Dianzi University, Hangzhou, China (e-mail:szhsxhsyf@hdu.edu.cn, czh345068@gmail.com, (22320210, gespringing)@hdu.edu.cn).

W. Deng is with National Cancer Center/National Clinical Research Center for Cancer/Cancer Hospital&Shenzhen Hospital, Chinese Academy of Medical Sciences and Peking Union Medical College, Shenzhen, China (email: ming861212@163.com).

J. Liu is with Central South University, Changsha, China (e-mail:liujin06@csu.edu.cn).

W. Min is with Yunnan University, Kunming, China (e-mail:minwenwen@ynu.edu.cn).

A. Elazab is with the School of Biomedical Engineering, Shenzhen University, Shenzhen, China and Computer Science Department, Misr Higher Institute for Commerce and Computers, Mansoura, Egypt (email:ahmed.elazab@yahoo.com).

X. Wan and C. Wang are with Shenzhen Research Institute of Big Data, Shenzhen, China (e-mail:wanyang@sribd.cn; cmwangalbert@gmail.com).

to identify and remove bony structures using image features in an unsupervised manner. Simkó *et al.* [8] introduced a clavicle suppression algorithm that produced a bone image from a gradient map, adjusted along the bone boundary. This generated bone image was then subtracted from the CXR images to obtain soft tissue images. Similarly, Juhasz *et al.* [9] applied an active shape model for segmenting anatomical structures in CXR images, effectively suppressing bone shadows. They implemented this model on the JSRT dataset [10], which remains the only publicly accessible dataset of its kind. However, statistical-based methods generally require precise segmentation and boundary annotations, which often lack rich semantic information regarding bony structures.

With advancements in neural networks, deep learning-based algorithms have increasingly been used for bone suppression in CXR images, generating soft tissue images effectively. These methods typically approach bone suppression as either an end-to-end image denoising task or focus on predicting the bone residual. Generally, end-to-end image denoising yields better bone suppression, but it may compromise detail preservation due to model limitations. Conversely, the bone residual prediction approach often produces impressive results in the generation of lesion and texture, although it struggles to completely remove bones. Yang *et al.* [11] developed a cascaded multi-scale Convolutional Neural Network (CNN) trained within the gradient domain of CXR images for this purpose. While the model demonstrated impressive performance, it failed to maintain high levels of perceptual and structural integrity. Similarly, Gusarev *et al.* [12] treated bones as noise, using a combination of autoencoder and deep CNN features to remove bone structures, though this led to image blurring. Inspired by Generative Adversarial Networks (GANs) [13], Zhou *et al.* [14] introduced a Multi-scale Conditional Adversarial Network (MCA-Net) aimed at producing soft tissue images while preserving key anatomical structures. To address the issue of inconsistent background intensity in gradient-based methods, Chen *et al.* [15] introduced a cascaded CNN into the wavelet domain. Rajaraman *et al.* [16] developed the ResNet-BS model for bone suppression in CXR images, validating its effectiveness through subsequent analytic tasks. Additionally, Liu *et al.* [17] proposed a bone suppression technique for lateral CXR images utilizing data rectification and distillation learning.

Diffusion models [18] have emerged as a novel class of generative models, adept at producing high-quality images. They effectively address challenges such as mode collapse and convergence issues that are often encountered with GANs. While diffusion models have shown impressive generative abilities in various image generation fields, they encounter specific challenges when applied to bone suppression:

- Diffusion models, compared to other generative models, are more computationally intensive due to their larger number of parameters and iterative processing steps. This high demand limits their application in high-resolution imaging. Consequently, in the context of bone suppression, diffusion models often produce images with lower resolution and less detail than needed for clinical applications [19].

- The training of diffusion models for denoising varies across different frequency components. Specifically, denoising mid- to high-frequency components is generally easier than addressing low-frequency components during the reverse process. This imbalance, coupled with the instability inherent in multi-step sampling, hampers the generation of low-frequency information. This often results in deviations in pixel intensities, affecting brightness and contrast, which can complicate the interpretation of the generated medical images [20].

To apply diffusion models to bone suppression, Chen *et al.* [21] introduced BS-Diff, which involves developing a conditional diffusion model in pixel space, enhanced with a Variational Auto-Encoder (VAE) as an improvement module. The cascade architecture used in BS-Diff helps mitigate some low-frequency discrepancies typical of diffusion models. However, the model still faces challenges in achieving adequate resolution and fine detail, alongside high computational demands. Moreover, utilizing the cascade architecture at the same resolution can lead to partial information loss while incurring additional computational costs. Consequently, the challenges associated with diffusion models in bone suppression remain only partially addressed.

Recently, Latent Diffusion Models (LDMs) [22] have emerged as an extension of diffusion models, operating in a lower-dimensional space to enable the synthesis of high-resolution images with reduced computational costs. By leveraging latent space, these models significantly decrease the number of parameters in the noise estimator network. Building on this innovation, we propose an end-to-end LDM-based framework for high-resolution bone suppression, called BS-LDM, which treats the task as CXR-guided image denoising to achieve effective bone suppression. To enhance detail preservation, we design a multi-level hybrid loss-constrained Vector-Quantized Generative Adversarial Network (VQGAN) [23], known as ML-VQGAN, for perceptual compression of high-resolution images. Additionally, to address discrepancies in low-frequency information generation, we introduce offset noise [24] into the noise addition process to correct luminance offset during image generation. We also propose a temporal adaptive thresholding strategy to resolve pixel saturation issues during the reverse process. To assess the clinical relevance of our framework in aiding lung disease diagnosis, we conducted a clinical evaluation focusing on image quality and diagnostic utility. The results demonstrated excellent image quality scores and significant diagnostic improvements, highlighting the clinical value of our approach. Furthermore, we compiled a high-quality bone suppression dataset named SZCH-X-Rays, featuring high-resolution paired CXR and DES soft tissue images from 818 patients, collected in collaboration with our partner hospital. We also processed 241 pairs of CXR and DES soft tissue images from the JSRT dataset, the largest open-source dataset for bone suppression, by performing operations like inversion and contrast adjustment to convert these images into negative formats more frequently used in clinical settings. Our primary contributions are summarized as follows:

- We introduce an end-to-end LDM-based framework for

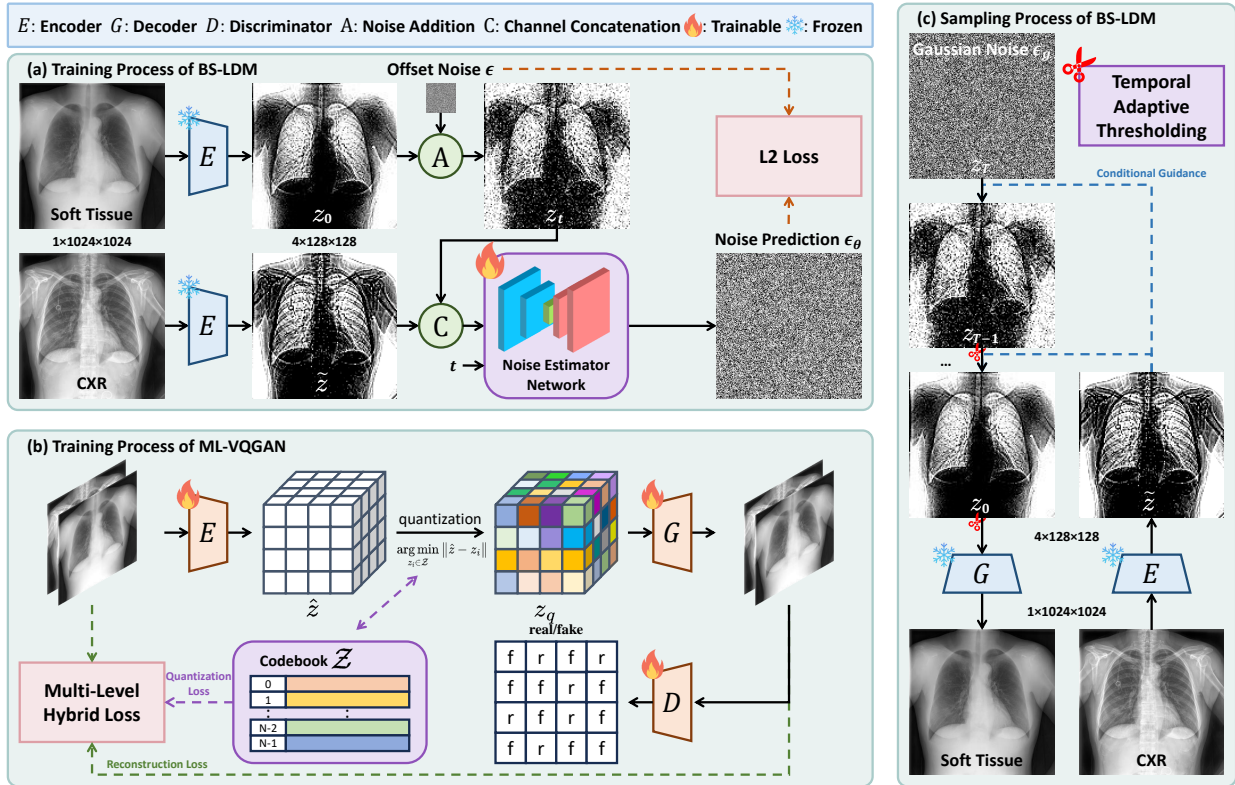


Fig. 1: Overview of the proposed BS-LDM: (a) The training process of BS-LDM, where CXR and noised soft tissue data in the latent space are transmitted to the noise estimator for offset noise prediction and L2 loss calculation; (b) The training process of ML-VQGAN, where a multi-level hybrid loss-constrained VQGAN is used to construct a latent space by training the reconstruction of CXR and soft tissue images, using a codebook to represent the discrete features of the images; (c) The sampling process of BS-LDM, where the latent variables obtained after each denoising step are clipped using a temporal adaptive thresholding strategy for the sake of contrast stability.

high-resolution bone suppression, named BS-LDM. It utilizes a multi-level hybrid loss-constrained VQGAN for effective perceptual compression. This framework consistently generates soft tissue images with high levels of bone suppression while preserving fine details and critical lung lesions.

- To enhance the quality of generated images, we incorporate offset noise and a temporal adaptive thresholding strategy. These innovations help minimize discrepancies in low-frequency information, thereby improving the interpretability of the soft tissue images.
- We have compiled a comprehensive bone suppression dataset, SZCH-X-Rays, which includes 818 pairs of high-resolution CXR and DES soft tissue images from our partner hospital. Additionally, we processed 241 pairs of images from the JSRT dataset into negative formats more commonly used in clinical settings.
- Our clinical evaluation focused on image quality and diagnostic utility. The results demonstrated excellent image quality scores and substantial diagnostic improvements, underscoring the clinical significance of our work.

II. METHODOLOGY

A. Overall Architecture

This section presents the proposed BS-LDM framework in detail. It is an end-to-end framework designed for effective bone suppression in high-resolution CXR images using a conditional LDM, as depicted in Fig. 1. In this framework, we developed a multi-level hybrid loss-constrained VQGAN for perceptual compression to ensure good detail preservation. Additionally, we incorporated offset noise and a temporal adaptive thresholding strategy to address discrepancies in low-frequency information generation, enhancing the overall quality of generation. A detailed description of each component of BS-LDM is provided in the following subsections.

B. Conditional Latent Diffusion Models

LDM-based approaches, such as Stable Diffusion [22], typically operate through a two-stage generative process. First, they map data to a low-dimensional latent space, and then sample from this space to generate the final output. Unlike traditional diffusion models like Denoising Diffusion Probabilistic Models (DDPMs) [18], LDMs significantly reduce computational demands for generating high-resolution images by encoding data in a compressed latent space. Specifically, for an image $x \in \mathbb{R}^{C \times H \times W}$, the encoder E transforms x into

a latent variable $z = E(x)$. In these models, a forward process, denoted as $q_\theta(z_t|z_0)$, is defined using a Markovian chain that gradually adds Gaussian noise to the input data z_0 :

$$z_t = \sqrt{\bar{\alpha}_t}z_0 + \sqrt{1 - \bar{\alpha}_t}\epsilon_g, \quad \epsilon_g \sim \mathcal{N}(\mathbf{0}, \mathbf{I}), \quad (1)$$

where ϵ_g is a noise map sampled from a Gaussian distribution, and $\bar{\alpha}_t := \prod_{s=0}^t \alpha_s$. Here, $\alpha_t = 1 - \beta_t$ is a differentiable function of timestep t determined by the denoising sampler. The diffusion training loss is formulated as:

$$\mathcal{L}(\epsilon_\theta) = \sum_{t=1}^T \mathbb{E}_{z_0, \epsilon_g} \left[\|\epsilon_\theta(\sqrt{\bar{\alpha}_t}z_0 + \sqrt{1 - \bar{\alpha}_t}\epsilon_g) - \epsilon_g\|_2^2 \right]. \quad (2)$$

In the context of conditional LDMs, with a given image condition \tilde{z} , the diffusion training loss at timestep t can be re-written as:

$$\mathcal{L}(\epsilon_\theta) = \mathbb{E}_{z_0, t, \tilde{z}, \epsilon_g} \left[\|\epsilon_\theta(z_t, t, \tilde{z}) - \epsilon_g\|_2^2 \right]. \quad (3)$$

During the reverse process, starting with random noise $z_T \sim \mathcal{N}(\mathbf{0}, \mathbf{I})$, the final denoised image x_0 is predicted through a step-by-step denoising process:

$$z_{t-1} = \frac{1}{\sqrt{\alpha_t}} \left(z_t - \frac{1 - \alpha_t}{\sqrt{1 - \bar{\alpha}_t}} \epsilon_\theta(z_t, t) \right) + \sigma_t \epsilon_g, \quad (4)$$

where ϵ_θ represents the predicted noise at timestep t by the noise estimator network with parameters θ , and $\sigma_t = \frac{1 - \bar{\alpha}_{t-1}}{1 - \bar{\alpha}_t} \beta_t$ is the variance of posterior Gaussian distribution $p_\theta(x_0)$.

In this work, we employ a U-Net [25] with multi-resolution attention [26] as the noise estimator network. The conditional guidance of CXR images in BS-LDM is achieved through the channel concatenation of z_t and \tilde{z} , as illustrated in Fig. 1 (a).

C. Multi-Level Hybrid Loss-Constrained VQGAN

To construct a low-dimensional latent space for LDMs while ensuring high-quality perceptual compression and reconstruction, we introduce a multi-level hybrid loss-constrained VQGAN, named ML-VQGAN, as shown in Fig. 1 (b). This approach compresses the pixel space $X \in \mathbb{R}^{1 \times H \times W}$ into a low-dimensional latent space $Z \in \mathbb{R}^{C \times \frac{H}{r} \times \frac{W}{r}}$ using ML-VQGAN. To prevent the creation of latent spaces with excessively high variance, VQ regularization is applied, allowing for the fine-tuning of latent features and achieving the final coding vectors z_q .

The total loss function for ML-VQGAN is defined as follows:

$$\mathcal{L}_{Total} = \mathcal{L}_{Recon} + \lambda_{Qua} \cdot \mathcal{L}_{Qua}, \quad (5)$$

where

$$\mathcal{L}_{Recon} = \lambda_{L1} \cdot \mathcal{L}_{L1} + \lambda_{Per} \cdot \mathcal{L}_{Per} + \lambda_{Adv} \cdot \mathcal{L}_{Adv}. \quad (6)$$

In this formulation, \mathcal{L}_{Recon} is a combination of multiple reconstruction losses at different levels. The weight coefficients λ_{Qua} , λ_{L1} , λ_{Per} , and λ_{Adv} adjust the influence of the respective components \mathcal{L}_{Qua} , \mathcal{L}_{L1} , \mathcal{L}_{Per} , and \mathcal{L}_{Adv} on the total loss.

1) **Reconstruction Loss:** To achieve high-quality image reconstruction, we incorporate L1 loss \mathcal{L}_{L1} , perceptual loss \mathcal{L}_{Per} [27], and adversarial loss \mathcal{L}_{Adv} [28] into the reconstruction loss \mathcal{L}_{Recon} . The L1 loss \mathcal{L}_{L1} evaluates the pixel-level differences between the reconstructed image and the original image, defined as:

$$\mathcal{L}_{L1} = \frac{1}{N} \sum_{i=1}^N |x_i - \hat{x}_i|. \quad (7)$$

To address the potential blurring effects of relying solely on pixel-level loss, we introduce the perceptual loss \mathcal{L}_{Per} , which uses features from pre-trained deep neural networks to enhance image quality:

$$\mathcal{L}_{Per} = \frac{1}{N} \sum_{k=1}^N (\phi_k(x) - \phi_k(\hat{x}))^2, \quad (8)$$

where ϕ_k denotes the k -th feature map extracted from a pre-trained deep neural network, which, in our study, is the VGG16 model [29].

Additionally, to produce more realistic images, we include the adversarial loss \mathcal{L}_{Adv} , which employs a discriminator network D to differentiate between real and generated images:

$$\mathcal{L}_{Adv} = -\mathbb{E}[\log D(G(x))], \quad (9)$$

where $D(G(x))$ represents the probability that generated data is perceived as real.

2) **Quantization Loss:** In ML-VQGAN, the concept of quantization loss, \mathcal{L}_{Qua} , as described by Tudosiu *et al.* [30], is used to optimize the codebook \mathcal{Z} . The mathematical expression for this loss is:

$$\mathcal{L}_{Qua} = \|sg(E(x)) - z_q\|_2^2 + \beta \|E(x) - sg(z_q)\|_2^2, \quad (10)$$

where sg signifies the stop-gradient operation, and β represents the weight used to balance the optimization between the encoder E and the codebook \mathcal{Z} .

D. Offset Noise

In the forward process of LDMs, each pixel gradually accumulates a small amount of independently and identically distributed (i.i.d.) Gaussian noise at each step. LDMs are trained to predict this noise after it has disrupted real images. However, we observe that low-frequency features are more resistant to Gaussian noise, as illustrated in Fig. 2. To understand this phenomenon, we calculated the power spectral densities of soft tissue images from SZCH-X-Rays, corresponding latent variables, and Gaussian noise at different frequencies, as shown in Fig. 3.

Our analysis revealed that the power spectral densities of the low-frequency components in both real images and latent variables are higher compared to mid- and high-frequency components. In contrast, Gaussian noise maintains balanced power spectral densities across all frequency bands. This imbalance may explain why low-frequency components are less susceptible to corruption during the noise addition process in diffusion models and LDMs. As a result, low-frequency

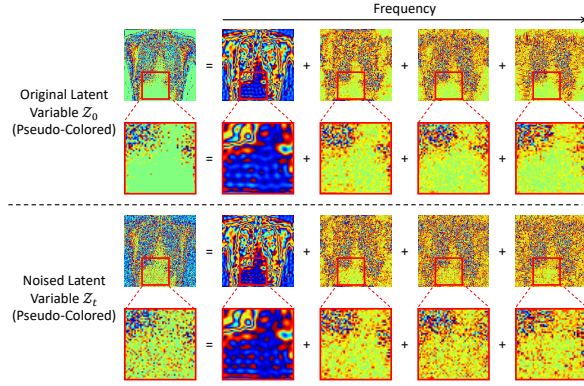


Fig. 2: Visualization of high-frequency and low-frequency feature decomposition of latent variables before and after Gaussian noise addition using Discrete Fourier Transform. The results are pseudo-colored for ease of demonstration.

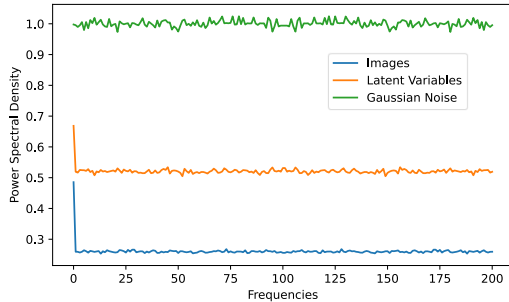


Fig. 3: Power spectral densities of soft tissue images in SZCH-X-Rays, corresponding latent variables and Gaussian noise on 201 spectrogram components, averaged over 10000 samples.

information is not entirely erased, leading to a noise signature that differs from standard Gaussian noise. Consequently, during the reverse process, which begins with Gaussian noise, there is a lack of consistency with the forward process. This inconsistency causes low-frequency information in generated images to resemble Gaussian noise rather than real images, potentially biasing the mean value of generated soft tissue images towards Gaussian noise. This bias can result in luminance discrepancies, reducing the interpretability of the images.

To resolve this issue, we introduce offset noise ϵ during the forward process, as depicted in Fig. 1 (a). This involves adding extra bias noise onto the standard noise addition procedure, as shown in Fig. 4 and formalized in (11):

$$z_t = \sqrt{\bar{\alpha}_t} z_0 + \sqrt{1 - \bar{\alpha}_t} \epsilon, \quad \epsilon \sim \mathcal{N}(0, \mathbf{I} + \lambda \cdot \Sigma), \quad (11)$$

where Σ is a covariance matrix of all ones, and λ is the weight of the bias noise. Bias noise is essentially zero-frequency noise, which can be derived from a one-pixel Gaussian noise using tensor broadcasting. The introduction of offset noise aims to completely eliminate the low-frequency information from real images during the noise addition process and ensure that the endpoints converge to true Gaussian noise. This modification broadens the spectrum of mean value variations in the generated images, thereby enhancing their resemblance to real images.

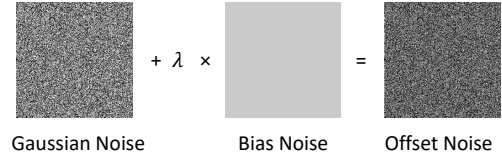


Fig. 4: Illustration of the composition of offset noise.

E. Temporal Adaptive Thresholding Strategy

In the reverse diffusion process, it is standard practice to constrain predicted values within the range of $[-1, 1]$ to maintain numerical stability. This approach, referenced in prior studies [18], has not received extensive attention. Saharia *et al.* referred to this as static thresholding and introduced a dynamic thresholding method to tackle the pixel saturation issues common in classifier-free guidance [31]. They employed a strategy where a threshold, s , was set to a particular percentile of the absolute pixel values, clipping data to $[-s, s]$ and normalizing by s if $s > 1$.

Although thresholding is typically absent in latent diffusion models [32], we observed that without it, these models are prone to pixel saturation, resulting in overly contrasted outputs. Static thresholding offers some numerical stability and reduces pixel saturation, but in our task, it severely restricted image variance, creating a marked contrast discrepancy between generated and real images. Similarly, while dynamic thresholding provides more flexibility, it still fails to adequately generate soft tissue images with clear interpretability.

To address these issues and align pixel intensities of generated soft tissue images with real ones, we propose a temporal adaptive thresholding strategy. This method dynamically adjusts the thresholding range $[-s, s]$ according to the current sampling step t . For the thresholding operation τ , we utilize a linear function to define the relationship between the threshold s and current sampling timestep t , as shown in (12):

$$\tau(z_{t,i}, s) = \begin{cases} -s, & \text{if } z_{t,i} < -s \\ z_{t,i}, & \text{if } -s \leq z_{t,i} \leq s, \quad s = \omega \cdot t + b, \quad (12) \\ s, & \text{if } z_{t,i} > s \end{cases}$$

where $z_{t,i}$ represents the i -th pixel of latent variable z_t at timestep t , $\omega (> 0)$ is the slope, and $b (\geq 1)$ is the intercept of the linear function.

By progressively expanding the thresholding range as the sampling evolves, temporal adaptive thresholding affords the model enhanced flexibility. This enables a nuanced adjustment of pixel intensities, ensuring the contrast of the final generated soft tissue images closely resembles that of real images.

III. EXPERIMENTS AND DISCUSSION

A. Data Preparation and Preprocessing

We compiled a dataset of 831 paired posterior-anterior CXR and DES soft tissue images. These images were acquired using a digital radiography system with a dual-exposure DES unit (Discovery XR656, GE Healthcare) from our partner hospital. Originally archived in 14-bit DICOM format, the images were converted to PNG format to simplify processing procedures.

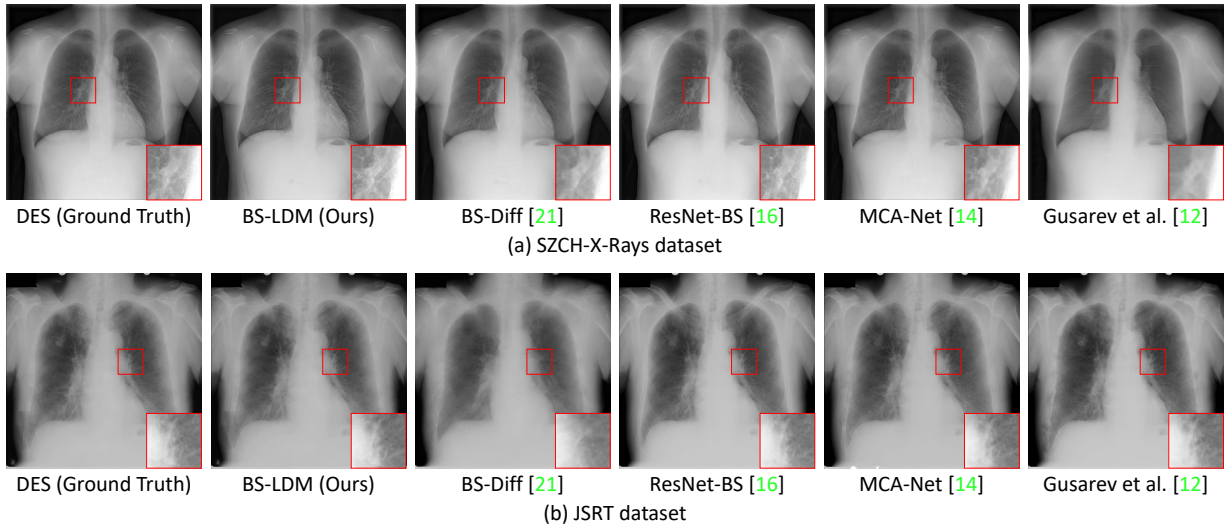


Fig. 5: Visualization of soft tissue images on SZCH-X-Rays and JSRT datasets produced by different methods.

Each image measures 2021×2021 pixels, with pixel sizes ranging from 0 to 0.1943 mm.

From this collection, we excluded 13 image pairs due to operational errors, severe motion artifacts, and conditions like pleural effusions and pneumothorax, which could interfere with analysis. The refined dataset, named SZCH-X-Rays, consists of 818 image pairs. These were divided into training, validation, and test sets in an 8:1:1 ratio. We enhanced local contrast in the images using contrast-limited adaptive histogram equalization.

Additionally, we processed 241 pairs of CXR and DES images from the JSRT dataset, the largest open-source collection available. Operations included inversion and contrast adjustment to convert them into negative images, commonly used in clinical practice. To optimize memory usage, images from both SZCH-X-Rays and JSRT datasets were resized to 1024×1024 pixels. Finally, all pixel values were normalized to the range $[-1, 1]$.

B. Implementation Details

All experiments were carried out using PyTorch 2.0.1 on a single Nvidia A100 80G GPU within Ubuntu 20.04 systems. We trained the ML-VQGAN model from scratch for 1,000 epochs with a batch size of 4, employing the Adam optimizer. Similarly, we trained our BS-LDM model from scratch for 2,500 epochs with a batch size of 4 using the AdamW optimizer, which required 22 hours.

For ML-VQGAN training, the loss weights were set to $\lambda_{L1} = \lambda_{Qua} = 1$, $\lambda_{Per} = 0.001$, and $\lambda_{Adv} = 0.01$, completing the process in approximately 20 hours. During BS-LDM training, we implemented an Exponential Moving Average (EMA) strategy with a decay coefficient of 0.995. We also employed a dynamic learning rate schedule, starting at 0.0001 for the ML-VQGAN encoder E and decoder G , 0.0005 for the ML-VQGAN discriminator D , and 0.0002 for the BS-LDM noise estimator network.

For BS-LDM, the number of training and inference timesteps T was set to 1,000. The variance schedule parameter

β varied from 0.008 to 0.02, distributed across T timesteps using a cosine noise schedule. In the forward process, the weight of bias noise in offset noise, λ , was set at 0.1. In the reverse process, we adopted a time-adaptive thresholding strategy, selecting $\omega = 0.003$ and $b = 1.4$ for the linear function's slope and intercept, respectively.

C. Evaluation Metrics

Four metrics are used to assess the quality of bone suppression: the Bone Suppression Ratio (BSR) [33], Mean Squared Error (MSE), Peak Signal-to-Noise Ratio (PSNR) [34], and Learned Perceptual Image Patch Similarity (LPIPS) [35].

The BSR evaluates how effectively bone suppression is applied in CXR images. It measures the difference between the estimated soft tissue image, denoted as $\hat{\mathbf{S}}$, and the actual soft tissue image, \mathbf{S} , while considering the corresponding bone image \mathbf{B} . The BSR formula is expressed as follows:

$$BSR = 1 - \sum_{i=1}^N (\mathbf{S}_i - \hat{\mathbf{S}}_i)^2 / \sum_{i=1}^N \mathbf{B}_i^2, \quad (13)$$

where a BSR value of 1 indicates ideal performance.

In addition to BSR, we employ two common pixel-level metrics, MSE and PSNR, which assess the pixel-level discrepancies between the generated and actual soft tissue images.

To further evaluate the generation of detail from a perceptual standpoint, we utilize LPIPS. This metric measures perceptual similarity between two images by comparing features extracted from a pre-trained deep neural network. LPIPS is calculated as follows:

$$LPIPS = \frac{1}{N \cdot M \cdot F} \sum_{i=1}^N \sum_{j=1}^M \sum_{f=1}^F (\phi_{i,j,f}(\mathbf{S}) - \phi_{i,j,f}(\hat{\mathbf{S}}))^2, \quad (14)$$

where $N \cdot M$ represents the number of image patches, F denotes the number of feature channels in the selected network layer, and $\phi_{i,j,f}$ indicates the features at position (i, j) and channel f .

D. Comparisons

To ensure an unbiased evaluation, we compared our proposed model with the leading ones recently highlighted in the literature. Specifically, we assessed our model against: an autoencoder-based model [12], the GAN-based MCA-Net [14], the ResNet-based ResNet-BS [16], and the diffusion model-based BS-Diff [21].

For consistency, we used the default parameters from the open-source implementations of these models and maintained the same resolution across all experiments. The comparative performance of these bone suppression techniques is shown for the SZCH-X-Rays and JSRT datasets in Table I and visually represented in Fig. 5.

1) *Evaluation on the SZCH-X-Rays Dataset*: In our SZCH-X-Rays dataset, our method outperforms all other approaches in terms of BSR (1.0% \uparrow), MSE (14.3% \downarrow), PSNR (1.047dB \uparrow), and LPIPS (34.6% \downarrow). This improvement is highlighted by significantly better retention of lung details, as demonstrated by a notable reduction in LPIPS of at least 35.6%, along with the detailed illustrations in Fig. 5 (a). The autoencoder-based model and BS-Diff exhibit poor performance across most evaluation metrics, primarily due to a substantial loss of texture. While MCA-Net and ResNet-BS maintain fair detail retention, they still lag behind BS-LDM because of slight differences in brightness and detail. Notably, all evaluated methods achieve effective bone suppression, with a BSR of at least 94.4%.

2) *Evaluation on the JSRT Dataset*: On the public JSRT dataset, our method similarly surpasses all other approaches in BSR (0.6% \uparrow), MSE (12.5% \downarrow), PSNR (0.375dB \uparrow) and LPIPS (64.7% \downarrow). The results shown in Fig. 5 (b) reveal sharper details in the BS-LDM outputs, particularly when compared to BS-Diff and the autoencoder-based model. However, the differences are less pronounced than those observed in the SZCH-X-Rays dataset due to the inherent blurring in the JSRT dataset. From a quantitative perspective, BS-LDM achieves significantly lower LPIPS on the JSRT dataset, indicating a higher perceptual quality of the generated soft tissue images. Despite generally fair performance across several metrics, ResNet-BS shows poor bone suppression in the clavicular area, as illustrated in Fig. 5 (b). The autoencoder-based model, MCA-Net, and BS-Diff perform poorly on most metrics, primarily due to slight pixel-level luminance differences and lack of detail.

E. Ablation Study

To evaluate the importance of offset noise and the temporal adaptive thresholding strategy within the BS-LDM framework, we conducted experiments by training the model with and without these components on SZCH-X-Rays and JSRT datasets. When offset noise was absent, we applied Gaussian noise for evaluation. When temporal adaptive thresholding was absent, we applied static thresholding, dynamic thresholding, and no thresholding to evaluate their effects. Our results indicate that incorporating both offset noise and temporal adaptive thresholding is crucial for producing accurate soft

tissue images, as it allows for better adjustment of low-frequency information. The quantitative data supporting these findings are presented in Table II, and the visual results can be seen in Fig. 6.

1) *Offset Noise Effect*: In examining the effectiveness of offset noise, we found that its application resulted in generated soft tissue images with mean values more aligned with real images. This adjustment led to a reduction in MSE by at least 92.5%, an improvement in PSNR by at least 0.897 dB, and a decrease in LPIPS by at least 3.8% compared to images generated without offset noise, across both datasets. Fig. 6 highlights that without offset noise, the brightness of the generated images was significantly misaligned.

2) *Temporal Adaptive Thresholding Effect*: Regarding temporal adaptive thresholding, expanding the thresholding range during sampling allowed for more precise adjustments of pixel intensities, as shown in Fig. 6. Numerically, this method improved image contrast consistency with real images, achieving a reduction in MSE by at least 92.5%, a PSNR increase of at least 0.897 dB, and a decrease in LPIPS by at least 3.8% compared to other thresholding strategies or the absence of thresholding. In contrast, Fig. 6 illustrates that static and dynamic thresholding severely limited image variance, while the lack of thresholding resulted in excessive contrast due to pixel saturation issues.

F. Hyperparameter Analysis

1) *Hyperparameter Analysis on the ML-VQGAN Loss*: We conducted a detailed analysis for each dataset to further examine the effects of the multi-level hybrid loss function of ML-VQGAN under varying hyperparameter settings. The results, as depicted in Table III and Table IV, reveal that the BS-LDM framework achieves optimal performance when the weight parameters λ_{L1} , λ_{Qua} , λ_{Per} , and λ_{Adv} are set to 1, 1, 0.001, and 0.01, respectively.

2) *Importance of Parameters on Offset Noise and Temporal Adaptive Thresholding*: To further investigate the impact of offset noise and the temporal adaptive thresholding strategy, we conducted a hyperparameter analysis on each dataset. The results, shown in Fig. 7, suggest that optimal model performance is achieved when the bias noise weight λ in offset noise is set to 0.1, and the parameters ω and b for temporal adaptive thresholding are set to 0.003 and 1.4, respectively. In offset noise, a large λ can disproportionately alter the model's behavior, whereas a small λ may render the effect negligible. Similarly, in the temporal adaptive thresholding strategy, the values of ω and b are influenced by the data characteristics, and extreme values can lead to a decline in performance.

G. Clinical Evaluation

1) *Image Quality Assessment*: The soft tissue images generated by the BS-LDM on the SZCH-X-Rays dataset were independently evaluated for image quality using established clinical criteria [36], [37] that are commonly applied to assess bone suppression efficacy. Three radiologists, with 6, 11, and 21 years of experience respectively, conducted these evaluations at our partner hospital. The detailed results are presented

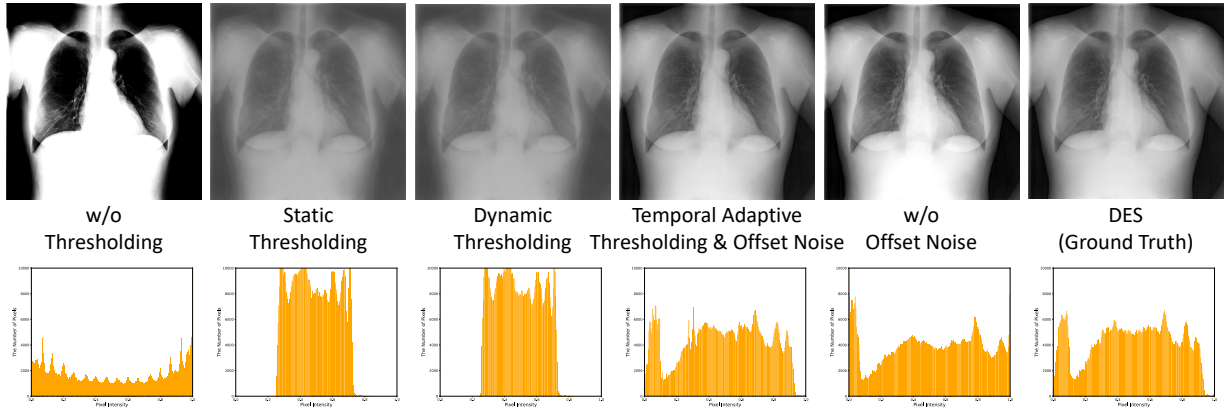


Fig. 6: Visualization of ablation studies of offset noise and the temporal adaptive thresholding strategy on BS-LDM, with histograms given to visualize the pixel intensity distribution more intuitively.

TABLE I: Comparison on SZCH-X-Rays and JSRT datasets with the state-of-the-art methods using BSR, MSE, PSNR and LPIPS as evaluation metrics.

Dataset	Method	BSR (\uparrow)	MSE (\downarrow)	PSNR (\uparrow)	LPIPS (\downarrow)
SZCH-X-Rays	Gusarev <i>et al.</i> [12]	0.944 \pm 0.018	0.0008 \pm 0.0002	31.900 \pm 3.449	0.220 \pm 0.012
	MCA-Net [14]	0.945 \pm 0.019	0.0007 \pm 0.0002	32.177 \pm 2.912	0.118 \pm 0.011
	ResNet-BS [16]	0.956 \pm 0.021	0.0009 \pm 0.0003	31.950 \pm 3.097	0.078 \pm 0.008
	BS-Diff [21]	0.971 \pm 0.022	0.0008 \pm 0.0004	31.057 \pm 3.585	0.191 \pm 0.015
	BS-LDM (Ours)	0.976 \pm 0.018	0.0006 \pm 0.0003	33.224 \pm 3.577	0.051 \pm 0.016
JSRT	Gusarev <i>et al.</i> [12]	0.865 \pm 0.041	0.0009 \pm 0.0002	31.216 \pm 2.255	0.193 \pm 0.017
	MCA-Net [14]	0.892 \pm 0.039	0.0009 \pm 0.0002	33.735 \pm 1.578	0.148 \pm 0.017
	ResNet-BS [16]	0.903 \pm 0.038	0.0009 \pm 0.0003	32.009 \pm 1.653	0.139 \pm 0.020
	BS-Diff [21]	0.902 \pm 0.032	0.0008 \pm 0.0003	33.937 \pm 2.465	0.147 \pm 0.024
	BS-LDM (Ours)	0.908 \pm 0.029	0.0007 \pm 0.0002	34.312 \pm 2.176	0.049 \pm 0.018

TABLE II: Ablation performance on SZCH-X-Rays and JSRT datasets using three evaluation metrics.

Offset Noise	Thresholding Strategy	SZCH-X-Rays			JSRT		
		MSE (\downarrow)	PSNR (\uparrow)	LPIPS (\downarrow)	MSE (\downarrow)	PSNR (\uparrow)	LPIPS (\downarrow)
\times	\times	0.1131	30.054	0.553	0.2619	28.109	0.918
\times	Static Thresholding	0.0164	30.222	0.141	0.0140	28.525	0.083
\times	Dynamic Thresholding	0.0161	30.319	0.142	0.0123	29.368	0.081
\times	Temporal Adaptive Thresholding	<u>0.0080</u>	<u>31.557</u>	<u>0.053</u>	<u>0.0109</u>	<u>33.415</u>	<u>0.053</u>
\checkmark	\times	0.1105	30.056	0.549	0.2590	28.104	0.809
\checkmark	Static Thresholding	0.0106	31.441	0.128	0.0140	28.525	0.083
\checkmark	Dynamic Thresholding	0.0103	29.937	0.130	0.0153	29.040	0.072
\checkmark	Temporal Adaptive Thresholding	0.0006	33.224	0.051	0.0007	34.312	0.049

TABLE III: Impact of different weight schemes of the multi-level hybrid loss function on SZCH X-Rays dataset.

Weight Scheme *	MSE (\downarrow)	PSNR (\uparrow)	LPIPS (\downarrow)
[1, 1, 1, 10^{-2}]	0.00073	30.013	0.040
[1, 1, 0, 10^{-2}]	0.00063	32.976	0.133
[1, 1, 10^{-1} , 10^{-2}]	0.00076	29.462	0.052
[1, 1, 10^{-2} , 10^{-2}]	0.00062	32.525	0.057
[1, 1, 10^{-3}, 10^{-2}]	0.00060	33.224	0.051
[1, 1, 10^{-3} , 10^{-1}]	0.00061	33.199	0.144
[1, 1, 10^{-3} , 0]	0.00062	32.845	0.142
[1, 1, 10^{-3} , 1]	0.00076	29.673	0.196

* λ_{L1} , λ_{Qua} , λ_{Per} and λ_{Adv} , from left to right.

TABLE IV: Impact of different weight schemes of the multi-level hybrid loss function on JSRT dataset.

Weight Scheme *	MSE (\downarrow)	PSNR (\uparrow)	LPIPS (\downarrow)
[1, 1, 1, 10^{-2}]	0.00098	30.261	0.051
[1, 1, 0, 10^{-2}]	<u>0.00072</u>	<u>34.167</u>	0.103
[1, 1, 10^{-1} , 10^{-2}]	0.00090	30.302	0.054
[1, 1, 10^{-2} , 10^{-2}]	0.00078	33.276	0.059
[1, 1, 10^{-3}, 10^{-2}]	0.00071	34.312	0.049
[1, 1, 10^{-3} , 10^{-1}]	0.00073	33.060	0.113
[1, 1, 10^{-3} , 0]	0.00073	33.714	0.119
[1, 1, 10^{-3} , 1]	0.00101	31.427	0.137

* λ_{L1} , λ_{Qua} , λ_{Per} and λ_{Adv} , from left to right.

in Table V. The average scores for lung vessel visibility, airway visibility, and the degree of bone suppression were 2.758, 2.714, and 2.765, respectively, out of a maximum score of 3. These findings indicate that BS-LDM effectively suppresses

bone while preserving fine details and lung pathology.

2) *Diagnostic Utility Assessment*: The diagnostic value of soft tissue imaging was independently evaluated by two radiologists with 6 and 11 years of experience, following the X-ray

TABLE V: Image quality assessment of BS-LDM scored by three radiologists with various levels of experience.

Clinical Evaluation Criteria		Junior Radiologist (6 years)	Intermediate Radiologist (11 years)	Senior Radiologist (21 years)
Lung vessel visibility	Clearly displayed (3) Displayed (2) Not displayed (1)	2.431	2.858	2.984
Airway visibility	Lobar and intermediate bronchi (3) Main bronchus and rump (2) Trachea (1)	2.561	2.643	2.937
Degree of bone suppression	Nearly perfect suppression (3) Unsuppressed bones less than 5 (2) 5 or more bones unsuppressed (1)	2.781	2.793	2.722

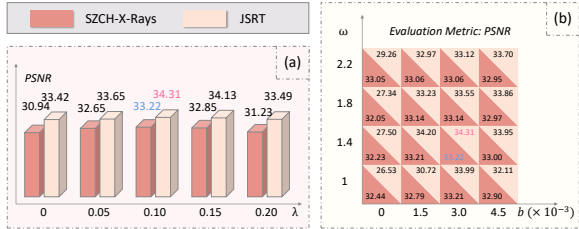


Fig. 7: Visualization of hyperparameter analysis of offset noise in (a) and the temporal adaptive thresholding strategy in (b) on SZCH-X-Rays and JSRT datasets.

TABLE VI: Diagnostic utility assessment of BS-LDM calculated from the diagnostic results of two radiologists with 6 and 11 years of experience, respectively.

Junior Radiologist	Precision (\uparrow)	Recall (\uparrow)	F1 Score (\uparrow)
CXR	0.70	0.40	0.51
Tissue	0.73	0.56	0.63
Senior Radiologist	Precision (\uparrow)	Recall (\uparrow)	F1 Score (\uparrow)
CXR	0.74	0.51	0.60
Tissue	0.75	0.75	0.75

diagnosis standard [38]. This analysis employed the SZCH-X-Rays dataset for bone suppression, using computed tomography to confirm lesions, which included common lung diseases such as inflammation, tuberculosis, and masses or nodules. Out of 818 data pairs assessed, 79 pairs contained one or more of these lesions. The radiologists independently evaluated both conventional CXR and the soft tissue images generated by our model. Table VI presents the results, highlighting key metrics such as Precision, Recall, and the F1 Score. The findings suggest that the soft tissue images produced by BS-LDM enable more thorough and accurate lesion diagnosis compared to CXR images, thereby confirming its high clinical diagnostic value.

H. Limitations

While BS-LDM demonstrates exceptional performance in suppressing bone structures and generating high-resolution CXR images, several limitations remain, and there are opportunities for further enhancements. For example, incorporating more advanced denoising samplers [32], [39] could help reduce the number of sampling steps needed. Additionally, adopting a mask-based approach might improve detail control

across different regions of the CXR images. Another potential improvement involves replacing the noise estimator network with alternatives, such as Transformer models [40] or Structured Space Models (SSM) [41], which could enhance the model’s flexibility and scalability. Finally, the applicability of our method in downstream computerized analyses [42], [43] remains to be confirmed. In our future work, we plan to address these limitations and explore potential improvements.

IV. CONCLUSION

To enhance radiologists’ ability to detect lung lesions with greater precision and thoroughness, we introduce BS-LDM, an end-to-end framework for bone suppression in high-resolution CXR images, utilizing generative LDMs. We utilize a multi-level hybrid loss-constrained VQGAN for perceptual compression to ensure detail preservation. To further refine the framework’s performance, we incorporate offset noise and a temporal adaptive thresholding strategy. These enhancements help reduce discrepancies in generating low-frequency information, thereby enhancing the quality and interpretability of the soft tissue images produced. Our framework effectively generates soft tissue images that achieve high levels of bone suppression while retaining essential details and preserving the integrity of lung lesions. Rigorous experimental and clinical evaluations confirm BS-LDM’s exceptional bone suppression capabilities and its significant clinical utility.

V. COMPLIANCE WITH ETHICAL STANDARDS

This research was conducted retrospectively and following the principles of the Declaration of Helsinki, utilizing previously obtained chest X-ray images that had been anonymized before conducting analysis, thus posing no harm to patients. We applied for an informed consent waiver. Approval was granted by the Ethics Committee of Cancer Hospital & Shenzhen Hospital, Chinese Academy of Medical Sciences and Peking Union Medical College (No. JS2023-19-2).

REFERENCES

- [1] L. Pham, H. Phan, R. Palaniappan, A. Mertins, and I. McLoughlin, “Cnn-moe based framework for classification of respiratory anomalies and lung disease detection,” *IEEE Journal of Biomedical and Health Informatics*, vol. 25, no. 8, pp. 2938–2947, 2021.
- [2] S. B. Shuvo, S. N. Ali, S. I. Swapnil, T. Hasan, and M. I. H. Bhuiyan, “A lightweight cnn model for detecting respiratory diseases from lung auscultation sounds using emd-cwt-based hybrid scalogram,” *IEEE Journal of Biomedical and Health Informatics*, vol. 25, no. 7, pp. 2595–2603, 2020.

- [3] J. Austin, B. Romney, and L. Goldsmith, "Missed bronchogenic carcinoma: radiographic findings in 27 patients with a potentially resectable lesion evident in retrospect." *Radiology*, vol. 182, no. 1, pp. 115–122, 1992.
- [4] F. Li, T. Hara, J. Shiraishi, R. Engelmann, H. MacMahon, and K. Doi, "Improved detection of subtle lung nodules by use of chest radiographs with bone suppression imaging: receiver operating characteristic analysis with and without localization." *American Journal of Roentgenology*, vol. 196, no. 5, pp. W535–W541, 2011.
- [5] S. Chen and K. Suzuki, "Computerized detection of lung nodules by means of "virtual dual-energy" radiography," *IEEE Transactions on Biomedical Engineering*, vol. 60, no. 2, pp. 369–378, 2012.
- [6] P. Vock and Z. Szucs-Farkas, "Dual energy subtraction: principles and clinical applications," *European Journal of Radiology*, vol. 72, no. 2, pp. 231–237, 2009.
- [7] K. Suzuki, H. Abe, H. MacMahon, and K. Doi, "Image-processing technique for suppressing ribs in chest radiographs by means of massive training artificial neural network (mtann)," *IEEE Transactions on Medical Imaging*, vol. 25, no. 4, pp. 406–416, 2006.
- [8] G. Simkó, G. Orbán, P. Máday, and G. Horváth, "Elimination of clavicle shadows to help automatic lung nodule detection on chest radiographs," in *4th European Conference of the International Federation for Medical and Biological Engineering: ECIFMBE 2008 23–27 November 2008 Antwerp, Belgium*. Springer, 2009, pp. 488–491.
- [9] S. Juhász, A. Horváth, L. Nikhazy, G. Horváth, and Á. Horváth, "Segmentation of anatomical structures on chest radiographs," in *XII Mediterranean Conference on Medical and Biological Engineering and Computing 2010: May 27–30, 2010 Chalkidiki, Greece*. Springer, 2010, pp. 359–362.
- [10] J. Shiraishi, S. Katsuragawa, J. Ikezoe, T. Matsumoto, T. Kobayashi, K.-i. Komatsu, M. Matsui, H. Fujita, Y. Kodera, and K. Doi, "Development of a digital image database for chest radiographs with and without a lung nodule: receiver operating characteristic analysis of radiologists' detection of pulmonary nodules," *American Journal of Roentgenology*, vol. 174, no. 1, pp. 71–74, 2000.
- [11] W. Yang, Y. Chen, Y. Liu, L. Zhong, G. Qin, Z. Lu, Q. Feng, and W. Chen, "Cascade of multi-scale convolutional neural networks for bone suppression of chest radiographs in gradient domain," *Medical Image Analysis*, vol. 35, pp. 421–433, 2017.
- [12] M. Gusarev, R. Kuleev, A. Khan, A. R. Rivera, and A. M. Khattak, "Deep learning models for bone suppression in chest radiographs," in *2017 IEEE Conference on Computational Intelligence in Bioinformatics and Computational Biology (CIBCB)*. IEEE, 2017, pp. 1–7.
- [13] I. Goodfellow, J. Pouget-Abadie, M. Mirza, B. Xu, D. Warde-Farley, S. Ozair, A. Courville, and Y. Bengio, "Generative adversarial nets," *Advances in Neural Information Processing Systems*, vol. 27, 2014.
- [14] B. Zhou, X. Lin, B. Eck, J. Hou, and D. Wilson, "Generation of virtual dual energy images from standard single-shot radiographs using multi-scale and conditional adversarial network," in *Computer Vision—ACCV 2018: 14th Asian Conference on Computer Vision, Perth, Australia, December 2–6, 2018*. Springer, 2019, pp. 298–313.
- [15] Y. Chen, X. Gou, X. Feng, Y. Liu, G. Qin, Q. Feng, W. Yang, and W. Chen, "Bone suppression of chest radiographs with cascaded convolutional networks in wavelet domain," *IEEE Access*, vol. 7, pp. 8346–8357, 2019.
- [16] S. Rajaraman, G. Zamzmi, L. Folio, P. Alderson, and S. Antani, "Chest x-ray bone suppression for improving classification of tuberculosis-consistent findings," *Diagnostics*, vol. 11, no. 5, p. 840, 2021.
- [17] Y. Liu, F. Zeng, M. Ma, B. Zheng, Z. Yun, G. Qin, W. Yang, and Q. Feng, "Bone suppression of lateral chest x-rays with imperfect and limited dual-energy subtraction images," *Computerized Medical Imaging and Graphics*, vol. 105, p. 102186, 2023.
- [18] J. Ho, A. Jain, and P. Abbeel, "Denoising diffusion probabilistic models," *Advances in Neural Information Processing Systems*, vol. 33, pp. 6840–6851, 2020.
- [19] T. Weber, M. Ingrisch, B. Bischl, and D. Rügamer, "Cascaded latent diffusion models for high-resolution chest x-ray synthesis," in *Pacific-Asia Conference on Knowledge Discovery and Data Mining*. Springer, 2023, pp. 180–191.
- [20] O. A. M. F. Alnaggar, B. N. Jagadale, M. A. N. Saif, O. A. Ghaleb, A. A. Ahmed, H. A. A. Aqlan, and H. D. E. Al-Ariki, "Efficient artificial intelligence approaches for medical image processing in healthcare: comprehensive review, taxonomy, and analysis," *Artificial Intelligence Review*, vol. 57, no. 8, p. 221, 2024.
- [21] Z. Chen, Y. Sun, R. Ge, W. Qin, C. Pan, W. Deng, Z. Liu, W. Min, A. Elazab, X. Wan *et al.*, "Bs-diff: Effective bone suppression using conditional diffusion models from chest x-ray images," in *2024 IEEE International Symposium on Biomedical Imaging (ISBI)*. IEEE, 2024, pp. 1–5.
- [22] R. Rombach, A. Blattmann, D. Lorenz, P. Esser, and B. Ommer, "High-resolution image synthesis with latent diffusion models," in *Proceedings of the IEEE/CVF Conference on Computer Vision and Pattern Recognition*, 2022, pp. 10684–10695.
- [23] P. Esser, R. Rombach, and B. Ommer, "Taming transformers for high-resolution image synthesis," in *Proceedings of the IEEE/CVF Conference on Computer Vision and Pattern Recognition*, 2021, pp. 12873–12883.
- [24] N. Guttenberg, "Diffusion with offset noise," <https://www.crosslabs.org/blog/diffusion-with-offset-noise>, 2023.
- [25] O. Ronneberger, P. Fischer, and T. Brox, "U-net: Convolutional networks for biomedical image segmentation," in *Medical Image Computing and Computer-Assisted Intervention—MICCAI 2015: 18th International Conference, Munich, Germany, October 5–9, 2015, Proceedings, Part III 18*. Springer, 2015, pp. 234–241.
- [26] P. Dhariwal and A. Nichol, "Diffusion models beat gans on image synthesis," *Advances in Neural Information Processing Systems*, vol. 34, pp. 8780–8794, 2021.
- [27] J. Johnson, A. Alahi, and L. Fei-Fei, "Perceptual losses for real-time style transfer and super-resolution," in *Computer Vision—ECCV 2016: 14th European Conference, Amsterdam, The Netherlands, October 11–14, 2016, Proceedings, Part II 14*. Springer, 2016, pp. 694–711.
- [28] T.-C. Wang, M.-Y. Liu, J.-Y. Zhu, A. Tao, J. Kautz, and B. Catanzaro, "High-resolution image synthesis and semantic manipulation with conditional gans," in *Proceedings of the IEEE Conference on Computer Vision and Pattern Recognition*, 2018.
- [29] K. Simonyan and A. Zisserman, "Very deep convolutional networks for large-scale image recognition," *arXiv preprint arXiv:1409.1556*, 2014.
- [30] P.-D. Tudosiu, W. H. L. Pinaya, M. S. Graham, P. Borges, V. Fernandez, D. Yang, J. Appleyard, G. Novati, D. Mehra, M. Vella *et al.*, "Morphology-preserving autoregressive 3d generative modelling of the brain," in *International Workshop on Simulation and Synthesis in Medical Imaging*. Springer, 2022, pp. 66–78.
- [31] J. Ho and T. Salimans, "Classifier-free diffusion guidance," *arXiv preprint arXiv:2207.12598*, 2022.
- [32] C. Lu, Y. Zhou, F. Bao, J. Chen, C. Li, and J. Zhu, "Dpm-solver: A fast ode solver for diffusion probabilistic model sampling in around 10 steps," *Advances in Neural Information Processing Systems*, vol. 35, pp. 5775–5787, 2022.
- [33] L. Hogeweg, C. I. Sánchez, and B. van Ginneken, "Suppression of translucent elongated structures: applications in chest radiography," *IEEE Transactions on Medical Imaging*, vol. 32, no. 11, pp. 2099–2113, 2013.
- [34] A. Hore and D. Ziou, "Image quality metrics: Psnr vs. ssim," in *2010 20th International Conference on Pattern Recognition*. IEEE, 2010, pp. 2366–2369.
- [35] R. Zhang, P. Isola, A. A. Efros, E. Shechtman, and O. Wang, "The unreasonable effectiveness of deep features as a perceptual metric," in *Proceedings of the IEEE Conference On Computer Vision and Pattern Recognition*, 2018, pp. 586–595.
- [36] K. Bae, D. Y. Oh, I. D. Yun, and K. N. Jeon, "Bone suppression on chest radiographs for pulmonary nodule detection: comparison between a generative adversarial network and dual-energy subtraction," *Korean Journal of Radiology*, vol. 23, no. 1, p. 139, 2022.
- [37] G.-S. Hong, K.-H. Do, A.-Y. Son, K.-W. Jo, K. P. Kim, J. Yun, and C. W. Lee, "Value of bone suppression software in chest radiographs for improving image quality and reducing radiation dose," *European Radiology*, vol. 31, pp. 5160–5171, 2021.
- [38] T. Bansal and R. Beese, "Interpreting a chest x-ray," *British Journal of Hospital Medicine*, vol. 80, no. 5, pp. C75–C79, 2019.
- [39] S. Luo, Y. Tan, L. Huang, J. Li, and H. Zhao, "Latent consistency models: Synthesizing high-resolution images with few-step inference," *arXiv preprint arXiv:2310.04378*, 2023.
- [40] W. Peebles and S. Xie, "Scalable diffusion models with transformers," in *Proceedings of the IEEE/CVF International Conference on Computer Vision*, 2023, pp. 4195–4205.
- [41] Z. Fei, M. Fan, C. Yu, and J. Huang, "Scalable diffusion models with state space backbone," *arXiv preprint arXiv:2402.05608*, 2024.
- [42] C. Wang, A. Elazab, J. Wu, and Q. Hu, "Lung nodule classification using deep feature fusion in chest radiography," *Computerized Medical Imaging and Graphics*, vol. 57, pp. 10–18, 2017.
- [43] C. Wang, A. Elazab, F. Jia, J. Wu, and Q. Hu, "Automated chest screening based on a hybrid model of transfer learning and convolutional sparse denoising autoencoder," *Biomedical Engineering Online*, vol. 17, pp. 1–19, 2018.